Engineered Interfaces of Artificial Perovskite Oxide Superlattices *via* Nanosheet Deposition Process

Bao-Wen Li,[†] Minoru Osada,[†,‡,*] Tadashi C. Ozawa,[†,‡] Yasuo Ebina,[†,‡] Kosho Akatsuka,[†,‡] Renzhi Ma,[†,‡] Hiroshi Funakubo,[§] and Takayoshi Sasaki[†,‡]

[†]International Center for Materials Nanoarchitectonics (MANA), National Institute for Materials Science, Tsukuba, Ibaraki 305-0044, Japan, , [‡]CREST, Japan Science and Technology Agency, Kawaguchi, Saitama 332-0012, Japan, , and [§]Department of Innovative and Engineered Materials, Tokyo Institute of Technology, Yokohama 226-8502, Japan

ABSTRACT Combining different materials into desired superlattice structures can produce new electronic states at the interface and the opportunity to create artificial materials with novel properties. Here we introduce a new, rather unexpected, and yet simple way to such a superlattice assembly of perovskite oxides: in the Dion—Jacobson phase, a model system of layered perovskites, high-quality bicolor perovskite superlattices $(LaNb_2O_7)_{nL}(Ca_2Nb_3O_{10})_{nC}$ are successfully fabricated by a layer-by-layer assembly using two different perovskite nanosheets ($LaNb_2O_7$ and $Ca_2Nb_3O_{10}$) as a building block. The artificially fabricated ($LaNb_2O_7/Ca_2Nb_3O_{10}$) superlattices are structurally unique, which is not feasible to create in the bulk form. By such an artificial structuring, we found that ($LaNb_2O_7/Ca_2Nb_3O_{10}$) superlattices possess a new form of interface coupling, which gives rise to ferroelectricity.

KEYWORDS: perovskite nanosheets · layer-by-layer assembly · artificial superlattice · ferroelectricity

The development of advanced methods for a layer-by-layer growth of multicomponent perovskite superlattices has generated excitement,[1−3] both because of the intriguing physical phenomena that are not observable in bulk materials and because of potential applications in nonvolatile ferroelectric memories, piezoactuators, sensors, and magnetoelectric devices. These perovskite superlattices allow the tuning of physical properties while maintaining a perfect crystal structure, in practice, by forming a periodic sequence of ultrathin layers of different compounds, to observe emerging physical properties that are not necessarily a simple combination of those found in the constituent materials.[1,4−8] Underlying these studies is the technical prerequisite of the thin-film growth with single-unit-cell control and atomically sharp interfaces.[9,10] This has been usually achieved by laser molecular-beam expitaxy. However, current film-growth techniques require complex deposition processes with high-temperature postannealing, producing large extrinsic effects arising from growth-induced defects and/or thermal strain.[11] Thus, a key challenge in this field is the production of perovskite superlattices by engineering the interface at the atomic scale, which may realize the full potential of perovskite superlattices.

Recent advances in two-dimensional (2D) oxide nanosheets offer a new opportunity for room-temperature fabrication of oxide thin films.[12−16] Oxide nanosheets obtained *via* exfoliation of layered compounds possess a high 2D anisotropy with a molecular thickness (typically ∼1 nm) and, therefore, can be regarded as the thinnest self-standing 2D nanostructures having functionalities inherent from the parent compounds.[12] In addition, because of their polyelectrolytic nature, they can be employed as a building block for the electrostatic layer-by-layer self-assembly.[16] Research in such exotic 2D systems has recently intensified as a result of the emerging progress in graphene[17] as well as the successful exfoliation of transition-metal oxides including $Ti_{1-\delta}O_2$,[18,19] MnO_2,[20] and perovskite oxides.[13,21] In the perovskite case, the exfoliation of layered perovskites has been reported for Dion−Jacobson phases[13,21,22] including $LaNb_2O_7$, $(Ca,Sr)_2Nb_3O_{10}$, $CaLaNb_2TiO_{10}$, $La_2Ti_2NbO_{10}$, and for some others with Ruddlesden−Popper[13] ($SrLaTi_2TaO_{10}$, $Ca_2Ta_2TiO_{10}$) and Aurivillius ($SrBi_2Ta_2O_9$, $Bi_4Ti_3O_{12}$) phases.[23,24] An important aspect is that these nanosheets consist of perovskite building blocks of TiO_6, NbO_6, or TaO_6 octahedra. These features make the nanosheet an ideal base for high-*k* dielectrics and ferroelectrics with a critical thickness.[25,26] Therefore, the layer-by-layer

*Address correspondence to osada.minoru@nims.go.jp.

Received for review August 25, 2010 and accepted October 13, 2010.

Published online November 4, 2010. 10.1021/nn102144s

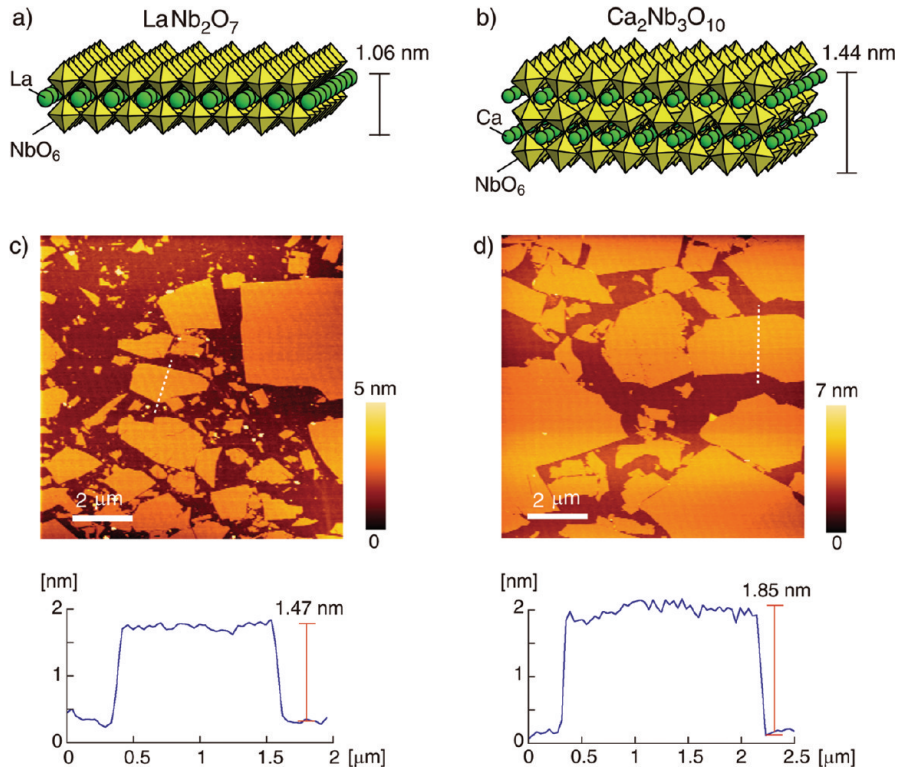

Figure 1. Structures and AFM images (10 × 10 μm^2) of $LaNb_2O_7$ (a,c) and $Ca_2Nb_3O_{10}$ (b,d) nanosheets. A tapping-mode AFM in vacuum condition was used to evaluate the morphology of the nanosheets on Si substrate. Height profiles are shown in the bottom panels.

approach for perovskite nanosheets could be useful for fabricating perovskite superlattices, but such possibilities have hardly been explored.

Here, we report on the fabrication and properties of high-quality bicolor perovskite superlattices, composed of two different perovskite nanosheets ($LaNb_2O_7$, $Ca_2Nb_3O_{10}$). These perovskite nanosheets are Dion−Jacobson phases with different perovskite-like layers (*m* octahedral thick). Natural superlattice structures with different *m* numbers do not exist in bulk form, and thus our superlattices with ($m = 2/m = 3$) nanosheets should be an intriguing type of artificial interface structure based on layered perovskites.

RESULTS AND DISCUSSION

Perovskite nanosheets ($LaNb_2O_7$, $Ca_2Nb_3O_{10}$) were prepared by delaminating layered perovskites according to previously described procedures.[21,22] The starting materials ($KLaNb_2O_7$, $KCa_2Nb_3O_{10}$) prepared by a solid-state reaction, were converted into their protonic forms ($HLaNb_2O_7 \cdot nH_2O$, $HCa_2Nb_3O_{10} \cdot 1.5H_2O$) in HNO_3 solution. Colloidal suspensions of perovskite nanosheets ($LaNb_2O_7$, $Ca_2Nb_3O_{10}$) were synthesized by delaminating these protonic forms with a tetrabutylammonium (TBA) hydroxide solution. This exfoliation process produced the colloidal suspension of monodispersed and unilamellar perovskite nanosheets, which are appropriate for the layer-by-layer self-assembly. Sectional analysis of atomic force microscopy (AFM) images (Figure 1) revealed a sheet-like morphology (with an average lateral dimension of a few μm), which is inherent to the host layer in the parent compounds. The average thicknesses were 1.47 ± 0.10 nm for $LaNb_2O_7$ and 1.85 ± 0.10 nm for $Ca_2Nb_3O_{10}$, respectively. The values obtained are nearly comparable to the crystallographic thickness of the host layer in the corresponding parent compounds, supporting the formation of unilamellar nanosheets.

We approached the preparation of superlattice films by the layer-by-layer assembly involving the Langmuir−Blodgett (LB) process[27] (Figure 2a). The LB isotherms for the colloidal suspensions showed a rise in the surface pressure without spreading amphiphilic additives (Figure 2b). This behavior was commonly observed in other nanosheets such as $Ti_{1-\delta}O_2$ and $Cs_4W_{11}O_{36}$,[27,28] and can be ascribed to the moderate amphiphilic nature of TBA ions used as a delaminating agent. By controlling the surface pressure, surface coverage of perovskite nanosheets was manipulated to give a uniform deposition (Supporting Information, Figures S1 and S2). In $LaNb_2O_7$ and $Ca_2Nb_3O_{10}$ cases, the best results were obtained for LB transfer at the surface pressure of 15 mN m^{-1}, yielding 95% coverage with only occasional overlaps and gaps. Below 15 mN m^{-1}, the nanosheets were loosely packed with noticeable gaps between them. In contrast, when exceeding 15 mN m^{-1}, overlapped patches of nanosheets started to form, suggesting the collapsed texture of the films. On

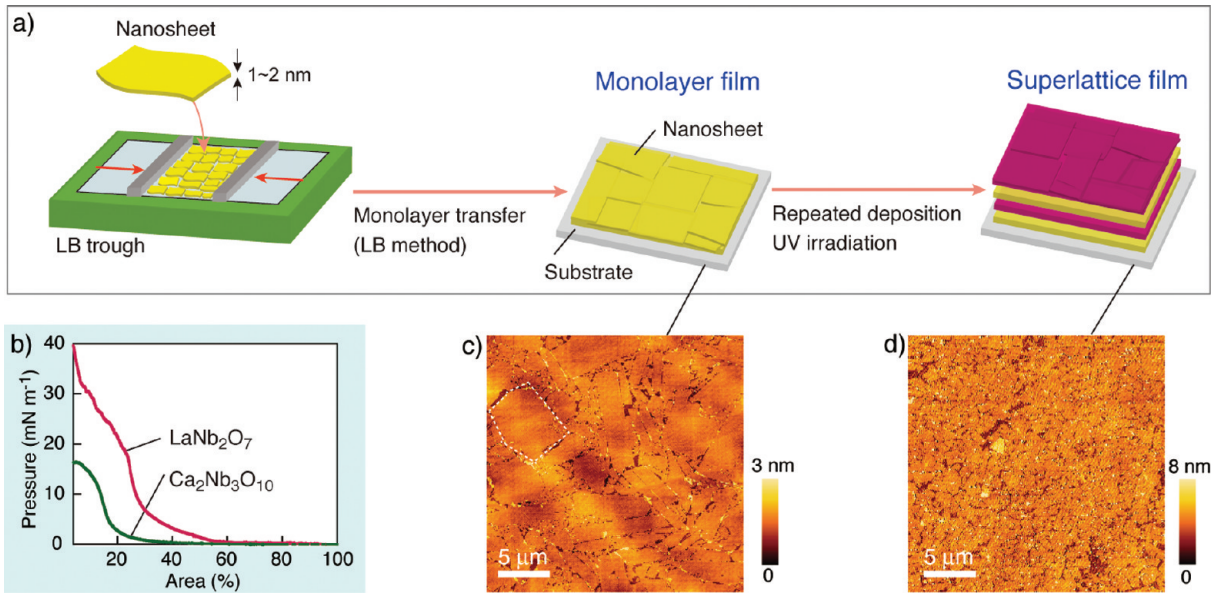

Figure 2. (a) Fabrication procedure for superlattice films using the LB method. (b) Pressure−area (π−A) isotherms for nanosheet suspensions ($LaNb_2O_7$ and $Ca_2Nb_3O_{10}$) at 25 °C. For the horizontal axis, the percentage of surface area relative to the area before compression is used. (c, d) AFM images (25 × 25 μm^2) of $Ca_2Nb_3O_{10}$ monolayer film and $(LaNb_2O_7/Ca_2Nb_3O_{10})_2$ superlattice on $SrRuO_3$ substrate. A selected nanosheet is outlined for clarity.

the basis of the results, the surface pressure of 15 mN m^{-1} was selected as the optimal condition for the well-organized LB films.

The procedure for the LB depositions involving two or more different nanosheets was repeated an appropriate number of times to synthesize the superlattice assembly. The use of an atomically flat $SrRuO_3$ substrate is effective for the fabrication of an atomically uniform superlattice film with a highly dense characteristic. Figure 2a illustrates such an example in $(LaNb_2O_7/Ca_2Nb_3O_{10})_2$ superlattice on a $SrRuO_3$ substrate. An AFM image (Figure 2c) revealed that the $Ca_2Nb_3O_{10}$ monolayer film appeared flat at the atomic scale and uniform over a large area; the roughness (root-mean-square) was ~0.3 nm. Repeated LB transfer of the monolayer could yield superlattice films; the nearly perfect characteristics persist in thicker films (Figure 2d), indicating that the high-quality monolayer could be repeatedly deposited to yield a well-ordered lamellar structure in superlattice films. The as-deposited films were irradiated by ultraviolet (UV) light in order to decompose TBA ions used in the exfoliation process. Infrared absorption data revealed that the UV-treated films were successfully analyzed based on a multilayer-assembly model composed of nanosheets and charge-balancing cations such as NH_4^+ ions.

The layer-by-layer assembly process of nanosheets could be monitored by the UV−visible absorption spectra. Figure 3 panels a−d show the data when $LaNb_2O_7$ and $Ca_2Nb_3O_{10}$ nanosheets were deposited in four different sequences. The absorption peaks noticeable at 206 and 232 nm are attributable to $LaNb_2O_7$ and $Ca_2Nb_3O_{10}$ nanosheets, respectively, as is clear from the data for the multilayer films composed of each nanosheet (Figures 3e,f). In the superlattice films, each deposition cycle causes progressive enhancements for

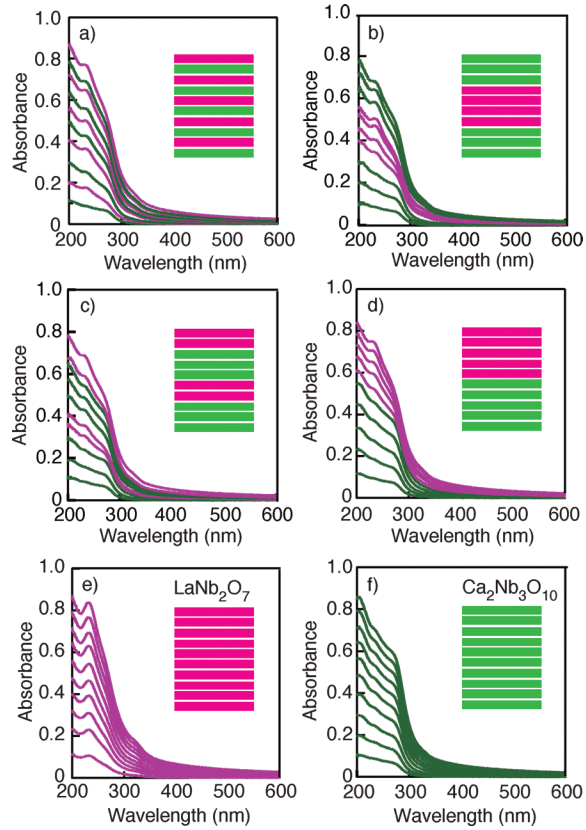

Figure 3. UV−visible absorption spectra in the multilayer buildup process. (a) $(LaNb_2O_7/Ca_2Nb_3O_{10})_5$, (b) $(Ca_2Nb_3O_{10})_3(LaNb_2O_7)_4(Ca_2Nb_3O_{10})_3$, (c) $(LaNb_2O_7)_2(Ca_2Nb_3O_{10})_3(LaNb_2O_7)_2(Ca_2Nb_3O_{10})_3$, (d) $(LaNb_2O_7)_5(Ca_2Nb_3O_{10})_5$, (e) $(LaNb_2O_7)_{10}$, (f) $(Ca_2Nb_3O_{10})_{10}$. Insets show schematic illustrations of superlattice structures where the purple and green blocks correspond to $LaNb_2O_7$ and $Ca_2Nb_3O_{10}$ nanosheets, respectively.

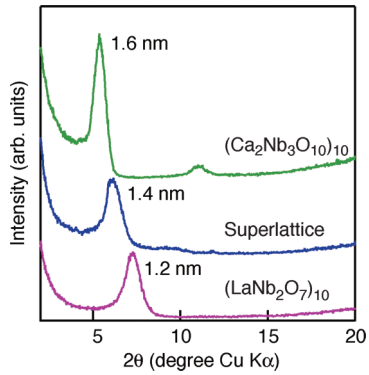

Figure 4. XRD pattern for $(LaNb_2O_7/Ca_2Nb_3O_{10})_5$ superlattice in comparison with those for multilayer films of $(LaNb_2O_7)_{10}$ and $(Ca_2Nb_3O_{10})_{10}$.

the superlattice-type buildup, and the spectral profile observed can be understood in terms of the superimposition of the profile of each nanosheet in the designed sequences.

Successful deposition of the superlattices was also confirmed by X-ray diffraction (XRD) (Figure 4). In the $(LaNb_2O_7/Ca_2Nb_3O_{10})_5$ superlattice, the XRD data exhibited a Bragg peak centered at $2\theta = 6.2°$. The d spacing of 1.4 nm for this peak is clearly different from the multilayer repeat distance for the films of each component of $LaNb_2O_7$ ($d = 1.2$ nm) and $Ca_2Nb_3O_{10}$ ($d = 1.6$ nm) nanosheets. Because the obtained value of $d = 1.4$ nm is close to half of the repeating unit of $LaNb_2O_7/Ca_2Nb_3O_{10}$ ($d = 2.8$ nm $= 1.2 + 1.6$ nm), the reflection observed for the superlattice may be interpreted as the second-order line for the superlattice. The apparent absence of the first-order peak may be explained by fairly similar scattering amplitudes of $LaNb_2O_7$ and $Ca_2Nb_3O_{10}$ nanosheets in the film. The intensity ratio of the first- and second-order lines was calculated as 100, 1 and 100, 10 for the multilayer films of $(LaNb_2O_7)_{10}$ and $(Ca_2Nb_3O_{10})_{10}$, respectively, whereas the values of 0, 100 were obtained for the $(LaNb_2O_7/Ca_2Nb_3O_{10})_5$ superlattice, which is in agreement with the observed profile.

Cross-sectional high-resolution transmission electron microscopy (HRTEM) observations (Figure 5) provide direct information on the superlattice formation. An image of the $(LaNb_2O_7/Ca_2Nb_3O_{10})_3$ superlattice (Figure 5a) revealed that the substrate surface is covered with the superlattice nanofilm, and the coverage and film thickness are homogeneous in a wide area. At a higher magnification (Figure 5b), the regular growth structure composed of $Ca_2Nb_3O_{10}$ and $LaNb_2O_7$ layers is clearly seen. The thickness of the constituent layers was approximately 1.6 and 1.2 nm, which are in good agreement with the crystallographic thickness of 1.44 nm for $Ca_2Nb_3O_{10}$ and 1.06 nm for $LaNb_2O_7$ nanosheets, respectively. In addition, there are no detectable stacking defects in the superlattice. These results clearly indicate that the alternating superlattice stacking of $Ca_2Nb_3O_{10}$ and $LaNb_2O_7$ nanosheets is maintained not only in nanometer scale but also in a wider-ranging area.

Electron energy-loss spectroscopy (EELS) in TEM was used to probe compositional changes at the interface (Figure 5c,d). Simultaneously recorded La-$N_{2,3}$ and Ca-$L_{2,3}$ edge spectra show a compositional abruptness between $SrRuO_3$ substrate and subsequently deposited nanosheets; a comparison with reference spectra from $LaNb_2O_7$ and $Ca_2Nb_3O_{10}$ (Supporting Information, Figure S3) indicates that the lamellar parts (points 3−7) are the heterostructure composed of $LaNb_2O_7$ and $Ca_2Nb_3O_{10}$. The integrated intensity profiles of the La-$N_{2,3}$ and Ca-$L_{2,3}$ edges (Figure 5c) clearly resolve a compositional modulation in the lamellar parts (points

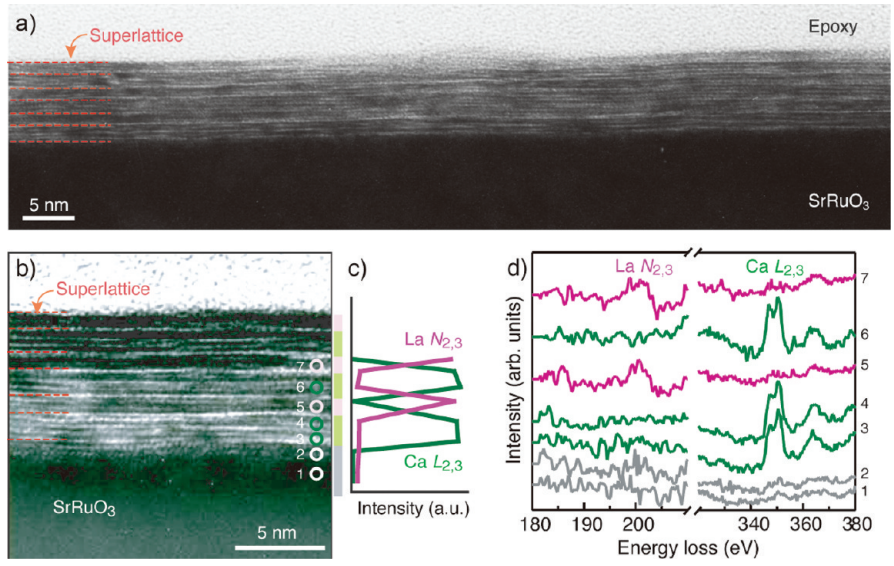

Figure 5. (a) HRTEM image and (b) higher magnification image of $(LaNb_2O_7/Ca_2Nb_3O_{10})_3$ superlattice on $SrRuO_3$ substrate. The dotted lines in the panels a and b are a guide for superlattice stackings. (c) The integrated intensity profiles of the La-$N_{2,3}$ and Ca-$L_{2,3}$ edges and (d) EELS spectra of the $(LaNb_2O_7/Ca_2Nb_3O_{10})_3$ superlattice. The electron beam position for these data is denoted by circles in panel b.

3−7); the Ca-$L_{2,3}$ and La-$N_{2,3}$ peaks alternately appeared at 1.6- and 1.2-nm steps. A clear benefit of our approach is the experimental realization of the atomically sharp interface between perovskite nanosheets and substrate. We note that there are no detectable interdiffusion and strains at the interface, suggesting the production of a dead-layer-free perovskite superlattice directly assembled on the $SrRuO_3$ substrate. Such a superior interface property is not specific to the superlattice geometry; the superlattice films of a similar quality were achieved in $(LaNb_2O_7)_{nL}(Ca_2Nb_3O_{10})_{nC}$ with different stacking sequences (n_L/n_C) and different substrates such as $SrTiO_3$:Nb or Pt, even by combining with other nanosheets (see Supporting Information, Figure S4). Therefore, our superlattice approach is quite general, and the exact control of interface atomic stackings can be realized in the self-assembled superlattices.

It is also noteworthy that the $(LaNb_2O_7/Ca_2Nb_3O_{10})$ superlattices are unique structures from the viewpoint of crystal chemistry. In Ruddlesden−Popper and Aurivillius phases, various intergrowth structures and natural superlattices (such as $Sr_{m+1}Ti_mO_{3m+1}$, $Bi_4Ti_3O_{12}$−$SrBi_4Ti_4O_{15}$, and Bi_3TiNbO_9−$Bi_4Ti_3O_{12}$) have been reported.[29−31] In Dion−Jacobson phases, however, the intergrowth structure with different m numbers does not naturally exist in the bulk form. Therefore, the $(LaNb_2O_7/Ca_2Nb_3O_{10})$ superlattices should be an intriguing type of artificial structure, where the different m structures of Dion−Jacobson phases are precisely assembled in the layer-by-layer fashion.

Now, questions rise whether modification of properties can be induced in such a self-assembled perovskite superlattice. This issue must be considered as important factors in the rational design of superlattices with engineered physical properties using nanosheets. In the case of typical superlattices, in which the in-plane lattice parameter of all the constituents is constrained to that of the underlying substrate, the primary interaction that determines the overall properties of the superlattice seems to be elastic; the principal consideration is the minimization of polarization mismatch between layers, any mismatch giving rise to very high electrostatic energy penalties. Thus, the elastic constraint imposed by the substrate is an important factor in determining the orientation of the polarization in the superlattice layers and thus has a dramatic effect on the properties of the superlattice.

In our case, the nanosheet superlattices are a unique system, in which the soft-chemical layer-by-layer approach does not restrict the elastic constraint imposed by the substrate, allowing an extraordinary opportunity for the exploration of the fundamentals of ferroelectricity. A possible indication comes from piezoelectric force microscopy (PFM), a powerful tool to characterize local ferroelectric properties in nanofilms and individual nanomaterials.[32] Figure 6 shows the PFM responses of three different superlattices as well as multilayer films

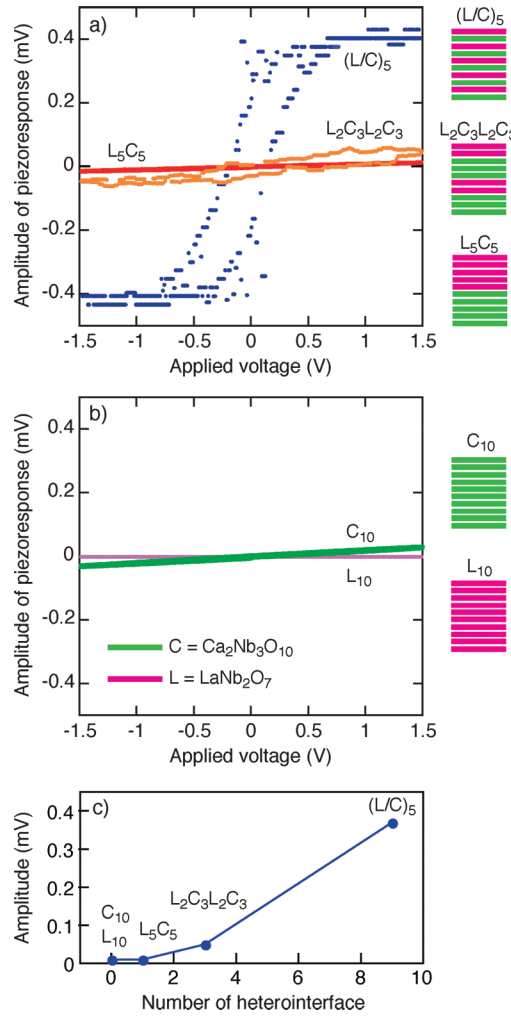

Figure 6. (a) PFM responses measured from different superlattices: $(LaNb_2O_7/Ca_2Nb_3O_{10})_5$ [$(L/C)_5$], $(LaNb_2O_7)_2(Ca_2Nb_3O_{10})_3(LaNb_2O_7)_2(Ca_2Nb_3O_{10})_3$ [$L_2C_3L_2C_3$], and $(LaNb_2O_7)_5(Ca_2Nb_3O_{10})_5$ [L_5C_5]. (b) PFM responses measured from multilayer films of $(LaNb_2O_7)_{10}$ [L_{10}] and $(Ca_2Nb_3O_{10})_{10}$ [C_{10}]. In panels a and b, the designed stacked structures are also indicated. (c) Relationship between the amplitude piezoresponse (at +1 V) and the number of the $LaNb_2O_7/Ca_2Nb_3O_{10}$ interfaces in the $(LaNb_2O_7)_{nL}(Ca_2Nb_3O_{10})_{nC}$ superlattices.

of $(LaNb_2O_7)_{10}$ and $(Ca_2Nb_3O_{10})_{10}$. The $(LaNb_2O_7/Ca_2Nb_3O_{10})_5$ superlattice shows a clear hysteresis behavior inherent to ferroelectricity, whereas multilayer films of $(LaNb_2O_7)_{10}$ and $(Ca_2Nb_3O_{10})_{10}$ reveal a paraelectric behavior. This observation points to a potential impact of the heterointerface on polarization properties in the superlattices.

Such an interfacial effect is also supported by the stacking dependence of the PFM response in the $(LaNb_2O_7)_{nL}(Ca_2Nb_3O_{10})_{nC}$ superlattices (Figure 6a,c). Clearly, the PFM response shows a strong dependence on the number of the $(LaNb_2O_7/Ca_2Nb_3O_{10})$ heterointerfaces in the superlattces; a sufficient number of the $(LaNb_2O_7/Ca_2Nb_3O_{10})$ heterointerfaces can modulate the PFM response, which is favorable for a stronger ferroelectricity. Thus, the ferroelectric response in Figure 6a is an intrinsic signature due to the interfacial effect

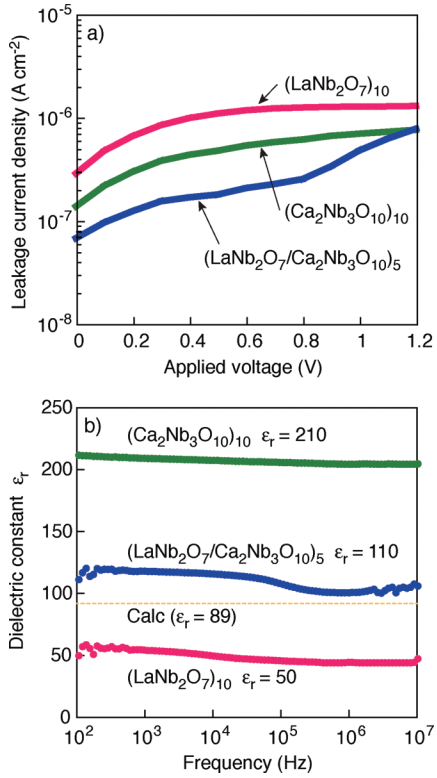

Figure 7. (a) *J*−*V* curves and (b) dielectric properties of $(LaNb_2O_7/Ca_2Nb_3O_{10})_5$ superlattice and multilayer films of $(LaNb_2O_7)_{10}$ and $(Ca_2Nb_3O_{10})_{10}$. In panel b, the estimated ε_r value from the parallel capacitor model is also indicated by a dotted line.

and not a consequence of the leakage current; the $(LaNb_2O_7/Ca_2Nb_3O_{10})_5$ superlattice exhibits a highly insulating nature with leakage current density of $<10^{-7}$ A cm^{-2} (Figure 7a).

Further evidence of the interfacial effect comes from the dielectric response in the $(LaNb_2O_7/Ca_2Nb_3O_{10})_5$ superlattice. Figure 7b shows the frequency dependence of the relative dielectric constant (ϵ_r) in the $(LaNb_2O_7/Ca_2Nb_3O_{10})_5$ superlattice together with the multilayer films of $(LaNb_2O_7)_{10}$ and $(Ca_2Nb_3O_{10})_{10}$. In the $(LaNb_2O_7/Ca_2Nb_3O_{10})_5$ superlattice, the ϵ_r values exhibited a small frequency dispersion in the regime of 100 Hz - 10 MHz, a behavior being similar to those observed in $(LaNb_2O_7)_{10}$ and $(Ca_2Nb_3O_{10})_{10}$. We note that the $(LaNb_2O_7/Ca_2Nb_3O_{10})_5$ shows an anomalously large

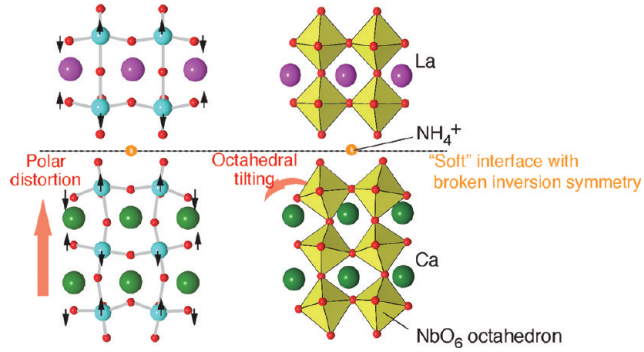

Figure 8. Schematic model of the $(LaNb_2O_7/Ca_2Nb_3O_{10})$ interface and motions associated to different energy lowering distortions.

ϵ_r response (~110) different from that of ordinary dielectrics. In the ordinary cases, the dielectric response in two component materials can be expressed by a series of the parallel capacitor model, and the ϵ_r value of the $(LaNb_2O_7/Ca_2Nb_3O_{10})_5$ superlattice can be accounted for by

$$\frac{t_{\text{superlattice}}}{\varepsilon_{\text{superlattice}}} = \frac{t_{LaNb_2O_7}}{\varepsilon_{LaNb_2O_7}} + \frac{t_{Ca_2Nb_3O_{10}}}{\varepsilon_{Ca_2Nb_3O_{10}}}$$

where t is the thickness of the dielectric component. The estimated ε_r value is 89, which is much smaller than the observed ε_r value (Figure 7b). This deviation in ε_r implies the possible existence of the interfacial effect on polarization properties in the $(LaNb_2O_7/Ca_2Nb_3O_{10})_5$ superlattice, in which the residual dipoles at the interface cause the enhanced polarization in the superlattice.

In bulk compounds $KLaNb_2O_7$ and $KCa_2Nb_3O_{10}$, that are precursors of $LaNb_2O_7$ and $Ca_2Nb_3O_{10}$ nanosheets, not only a polar zone-center distortion responsible for the ferroelectric ground state but also a zone-boundary distortion involving tilts of the oxygen octahedra are unstable. However, since $LaNb_2O_7$ and $Ca_2Nb_3O_{10}$ nanosheets are composed entirely of surface atoms arranged two-dimensionally, a zone-boundary distortion involving tilts of the oxygen octahedra can exist at the surface. In the multilayer cases, the polarization is nearly homogeneous across the whole film, which is electrostatically required to avoid large depolarizing fields. In the superlattice case, however, the asymmetric environment of the interfaces breaks the inversion symmetry, causing a polar zone-center distortion responsible for the ferroelectric state. Owing to the negatively charged character of nanosheets, neighboring nanosheets form a virtual dipole array, and the resultant depolarizing fields can further stabilize a polar zone-center distortion. Furthermore, the weak bonding of the adjoined nanosheets can facilitate a zone-boundary distortion involving tilts of the oxygen octahedra at the interface. In such a case, the ferroelectric/antiferrodistortive coupling is very strong at the interface, and such an interface effect produces a net coupling between the ferroelectric motion and the oxygen in-plane antiferrodistortive motion (Figure 8), a situation similar to the improper ferroelectricity observed in ferroelectric/paraelectric superlattices.[33] Although full understanding on ferroelectric character awaits further studies, our superlattice approach will offer an unprecedented opportunity for the realization of new interface states due to the "soft" interface coupling of electrostatic interaction, which cannot be found in current perovskite superlattices.

CONCLUSIONS

We successfully fabricated *m*-modulated bicolor superlattices through the LB process using two different perovskite nanosheets ($m = 2$ $LaNb_2O_7$, $m = 3$ $Ca_2Nb_3O_{10}$) as a building block. The formation of super-

lattice assemblies was confirmed by UV-vis absorption spectra, XRD, and HRTEM data. The artificially fabricated ($LaNb_2O_7/Ca_2Nb_3O_{10}$) superlattices are structurally unique and have a macroscopically homogeneous phase, which is not feasible to create in the bulk form. Another benefit of our approach is the experimental realization of the atomically sharp interface between perovskite nanosheet and substrate. The success of growth of such well-controlled superlattices with a good interface quality enabled us to explore new properties of perovskite superlattices, while eliminating interfacial degradation encountered in current film-growth techniques. By artificial structuring, we found that, in contrast to the paraelectric nature of $LaNb_2O_7$ and $Ca_2Nb_3O_{10}$, the ($LaNb_2O_7/Ca_2Nb_3O_{10}$) superlattice possesses a new form of interface coupling, which gives rise to ferroelectricity. The solution-based assembly of ferroelectric superlattices has a great potential for the rational design and construction of complex nanodevices and multiferroics, for example, by combining with ferromagnetic nanosheets.[34,35] Our work will open new opportunities for producing multiple superlattices by employing soft-chemical nanoarchitectonics based on 2D nanosheets.

METHODS

Sample Preparation. Colloidal suspensions of perovskite nanosheets ($LaNb_2O_7$, $Ca_2Nb_3O_{10}$) were prepared by delaminating layered perovskites ($KLaNb_2O_7$, $KCa_2Nb_3O_{10}$) according to previously described procedures (refs 21 and 22). An atomically flat conducting $SrRuO_3$ substrate, consisting of a 50-nm-thick (001)-oriented epitaxial $SrRuO_3$ film on a (001) $SrTiO_3$ single crystal, was used as a substrate. Before the film deposition, the substrate (1×1 cm^2) was photochemically cleaned using ultraviolet (UV) light irradiation in ozone. LB depositions of superlattice films were carried out using a USI FSD-3-777 double barrier LB trough equipped with a Wilhelmy-type balance for surface pressure measurement. The colloidal suspension of perovskite nanosheets was diluted with ultrapure water to concentrations of 0.03 g dm^{-3} ($LaNb_2O_7$) and 0.032 g dm^{-3} ($Ca_2Nb_3O_{10}$), and was placed in the LB trough at a regulated temperature of 25 $\pm$ 0.5 °C. After 30 min, the surface of the suspension started to compress at a rate of 0.5 mm s^{-1} until the surface pressure reached 15 mN m^{-1}. After maintaining a constant pressure for 30 min, the film at the interface was transferred onto the substrate through the vertical lifting of the substrate immersed in the LB trough at a transfer rate of 1.0 mm min^{-1}. After each LB deposition cycle, the film was dried at 110 °C for 20 min, and exposed to UV white light from a Xe lamp (1 mW cm^{-2}) for 30 min. The as-deposited films were irradiated by UV light for 24 h in order to totally decompose TBA ions used in the exfoliation process. We also fabricated reference films on Si and quartz glass substrates for sample characterization.

Characterization. The film quality of superlattice films was characterized by XRD, UV−visible absorption spectroscopy, AFM, and HRTEM. XRD patterns were collected by a Rigaku RINT 2200 powder diffractometer with monochromatized Cu Kα radiation (λ = 0.15405 nm). UV−visible absorption spectra were recorded in a transmission mode on a Hitachi U-4100 spectrophotometer. Film surface morphology was analyzed using an SII Nanotechnology E-sweep AFM. Cross-sectional HRTEM was carried out using a Hitachi H-9000 microscope operating at 200 kV, which has a point resolution of 0.1 nm.

XRD Analysis. X-ray diffraction patterns were calculated according to the following equation:

$$I(\theta) = \frac{1 + \cos^2 2\theta}{\sin^2 \theta \cos \theta} |F(\theta)|^2 \frac{\sin^2(2\pi Nd \sin \theta/\lambda)}{\sin^2(2\pi d \sin \theta/\lambda)}$$

$$F(\theta) = \sum_j f_j e^{2\pi i(2z_j \sin \theta/\lambda)}$$

where F is the structure factor, N is the number of the stacked unit structure, f_j is atomic scattering factor, d is the repeat distance, z_j is the atomic position along the sheet normal, and θ and λ are the diffraction angle and X-ray wavelength (=0.15405 nm). The intensity distribution was obtained using N = 10 for the multilayer assemblies, $(LaNb_2O_7)_{10}$ and $(Ca_2Nb_3O_{10})_{10}$, and N = 5 for the superlattice film, $(LaNb_2O_7/Ca_2Nb_3O_{10})_5$. Atomic parameters for each nanosheet were from previous reports (refs 21 and 22).

Electrical Characterization. PFM response was measured with a conducting tip (Rh-coated Si cantilever, $k \approx 1.6$ N m^{-1}) by an SII Nanotechnology E-sweep AFM. PFM responses were measured as a function of V_{dc} with a small ac voltage (0.5 V at 20 kHz) applied to the bottom electrode in the contact mode, and the resulting piezoelectric deformations transmitted to the cantilever were detected from the global deflection signal using a lock-in amplifier.

Electrical measurement was carried out by forming Au/(nanosheet)$_n$/$SrRuO_3$ capacitors. Au top electrodes (50-nm-thick, 100 μmϕ) were deposited using the vacuum evaporation method. Leakage current and dielectric properties were measured using a dielectric test system consisted of a semiconductor parameter analyzer (Keithley 4200-SCS) and a precision impedance analyzer (Agilent Technologies 4294A).

Acknowledgment. This work was in part supported by World Premier International Research Center Initiative on Materials Nanoarchitronics, MEXT, Japan. M.O. acknowledges support from the Industrial Technology Research Grant Program (06A22702d), NEDO, and the Grant-in-Aid for Scientific Research (208591), MEXT, Japan.

Supporting Information Available: Additional figures. This material is available free of charge *via* the Internet at http://pubs.acs.org.

REFERENCES AND NOTES

1. Ohtomo, A.; Hwang, H. Y. A High-Mobility Electron Gas at the $LaAlO_3/SrTiO_3$ Heterointerface. *Nature* **2004**, *427*, 423–426.
2. Hwang, H. Y. Atomic Control of the Electronic Structure at Complex Oxide Heterointerfaces. *MRS Bull.* **2006**, *31*, 28–35.
3. Mannhart, J.; Schlom, D. G. Oxide Interfaces-An Opportunity for Electronics. *Science* **2010**, *327*, 1607–1611.
4. Yamada, H.; Ogawa, Y.; Ishii, Y.; Sato, H.; Kawasaki, M.; Akoh, H.; Tokura, Y. Engineered Interface of Magnetic Oxides. *Science* **2004**, *305*, 646–648.
5. Lee, H. N.; Christen, H. M.; Chisholm, M. F.; Rouleau, C. M.; Lowndes, D. H. Strong Polarization Enhancement in Asymmetric Three-Component Ferroelectric Superlattices. *Nature* **2005**, *433*, 395–399.
6. Thiel, S.; Hammerl, G.; Schmehl, A.; Schneider, C. W.; Mannhart, J. Tunable Quasi-Two-Dimensional Electron Gases in Oxide Heterostructures. *Science* **2006**, *313*, 1942–1945.
7. Reyren, N.; Thiel, S.; Caviglia, A. D.; Kourkoutis, L. F.; Hammerl, G.; Richter, C.; Schneider, C. W.; Kopp, T.; Rüetschi, A. S.; Jaccard, D.; *et al*. Superconducting Interfaces between Insulating Oxides. *Science* **2007**, *317*, 1196–1199.

8. Brinkman, A.; Huijben, M.; Van Zalk, M.; Huijben, J.; Zeitler, U.; Maan, J. C.; Van der Wiel, W. G.; Rijnders, G.; Blank, D. H. A.; Hilgenkamp, H. Magnetic Effects at the Interface between Non-magnetic Oxides. *Nat. Mater.* **2007**, *6*, 493–496.
9. Kawasaki, M.; Takahashi, K.; Maeda, T.; Tsuchiya, R.; Shinohara, M.; Ishiyama, O.; Yonezawa, T.; Yoshimoto, M.; Koinuma, H. Atomic Control of the $SrTiO_3$ Crystal Surface. *Science* **1994**, *266*, 1540–1542.
10. Schlom, D. G.; Chen, L. Q.; Pan, X. Q.; Schmehl, A.; Zurbuchen, M. A. A Thin Film Approach to Engineering Functionality into Oxides. *J. Am. Ceram. Soc.* **2008**, *91*, 2429–2454.
11. Stengel, M.; Spaldin, N. A. Origin of the Dielectric Dead Layer in Nanoscale Capacitors. *Nature* **2006**, *443*, 679–682.
12. Sasaki, T.; Watanabe, M. Osmotic Swelling to Exfoliation. Exceptionally High Degrees of Hydration of a Layered Titanate. *J. Am. Chem. Soc.* **1998**, *120*, 4682–4689.
13. Schaak, R. E.; Mallouk, T. E. Perovskites by Design: A Toolbox of Solid-State Reactions. *Chem. Mater.* **2002**, *14*, 1455–1471.
14. Sasaki, T. Fabrication of Nanostructured Functional Materials Using Exfoliated Nanosheets as a Building Block. *J. Ceram. Soc. Jpn.* **2007**, *115*, 9–16.
15. Osada, M.; Sasaki, T. Exfoliated Oxide Nanosheets: New Solution to Nanoelectronics. *J. Mater. Chem.* **2009**, *19*, 2503–2511.
16. Sasaki, T.; Ebina, Y.; Tanaka, T.; Harada, M.; Watanabe, M.; Decher, G. Layer-by-Layer Assembly of Titania Nanosheet/Polycation Composite Films. *Chem. Mater.* **2001**, *13*, 4661–4667.
17. Novoselov, K. S.; Geim, A. K.; Morozov, S. V.; Jiang, D.; Zhang, Y.; Dubonos, S. V.; Grigorieva, I. V.; Firsov, A. A. Electric Field Effect in Atomically Thin Carbon Films. *Science* **2004**, *306*, 666–669.
18. Sasaki, T.; Watanabe, M.; Hashizume, H.; Yamada, H.; Nakazawa, H. Macromolecule-like Aspects for a Colloidal Suspension of an Exfoliated Titanate. Pairwise Association of Nanosheets and Dynamic Reassembling Process Initiated from It. *J. Am. Chem. Soc.* **1996**, *118*, 8329–8335.
19. Tanaka, T.; Ebina, Y.; Takada, K.; Kurashima, K.; Sasaki, T. Oversized Titania Nanosheet Crystallites Derived from Flux-Grown Layered Titanate Single Crystals. *Chem. Mater.* **2003**, *15*, 3564–3568.
20. Omomo, Y.; Sasaki, T.; Wang, L. Z.; Watanabe, M. Redoxable Nanosheet Crystallites of MnO_2 Derived *via* Delamination of a Layered Manganese Oxide. *J. Am. Chem. Soc.* **2003**, *125*, 3568–3575.
21. Ebina, Y.; Sasaki, T.; Watanabe, M. Study on Exfoliation of Layered Perovskite-type Niobates. *Solid State Ionics* **2002**, *151*, 177–182.
22. Ozawa, T. C.; Fukuda, K.; Akatsuka, K.; Ebina, Y.; Sasaki, T. Preparation and Characterization of the Eu^{3+} Doped Perovskite Nanosheet Phosphor: $La_{0.90}Eu_{0.05}Nb_2O_7$. *Chem. Mater.* **2007**, *19*, 6575–6580.
23. Ida, S.; Ogata, C.; Unal, U.; Izawa, K.; Inoue, T.; Altuntasoglu, O.; Matsumoto, Y. Preparation of a Blue Luminescent Nanosheet Derived from Layered Perovskite $Bi_2SrTa_2O_9$. *J. Am. Chem. Soc.* **2007**, *129*, 8956–8957.
24. Kim, J. Y.; Chung, I.; Choy, J. H.; Park, G. S. Macromolecular Nanoplatelet of Aurivillius-type Layered Perovskite Oxide, $Bi_4Ti_3O_{12}$. *Chem. Mater.* **2001**, *13*, 2759–2761.
25. Li, B. W.; Osada, M.; Ozawa, T. C.; Ma, R.; Akatsuka, K.; Ebina, Y.; Funakubo, H.; Ueda, S.; Kobayashi, K.; Sasaki, T. Solution-Based Fabrication of Perovskite Nanosheet Films and Their Dielectric Properties. *Jpn. J. Appl. Phys.* **2009**, *48*, 09KA15.
26. Osada, M.; Akatsuka, K.; Ebina, Y.; Funakubo, H.; Ono, K.; Takada, K.; Sasaki, T. Robust High-κ Response in Molecularly Thin Perovskite Nanosheets. *ACS Nano* **2010**, *4*, 5225–5232.
27. Akatsuka, K.; Haga, M.; Ebina, Y.; Osada, M.; Fukuda, K.; Sasaki, T. Construction of Highly Ordered Lamellar Nanostructures through Langmuir-Blodgett Deposition of Molecularly Thin Titania Nanosheets Tens of Micrometers Wide and Their Excellent Dielectric Properties. *ACS Nano* **2009**, *3*, 1097–1106.
28. Shibata, T.; Ohnishi, T.; Sakaguchi, I.; Osada, M.; Takada, K.; Kogure, T.; Sasaki, T. Well-Controlled Crystal Growth of Zinc Oxide Films on Plastics at Room Temperature Using 2D Nanosheet Seed Layer. *J. Phys. Chem. C* **2009**, *113*, 19096–19101.
29. Fisher, P.; Wang, S.; Skowronski, M.; Salvador, P. A.; Snyder, M.; Maksimov, O. A Series of Layered Intergrowth Phases Grown by Molecular Beam Epitaxy: Sr_mTiO_{2+m} ($m = 1-5$). *Appl. Phys. Lett.* **2007**, *91*, 252901.
30. Noguchi, Y.; Miyayama, M.; Kudo, T. Ferroelectric Properties of Intergrowth $Bi_4Ti_3O_{12}-SrBi_4Ti_4O_{15}$ Ceramics. *Appl. Phys. Lett.* **2000**, *77*, 3639–3641.
31. Shibuya, A.; Ikemori, S.; Wu, W. B.; Noda, M.; Okuyama, M. Preparation and Basic Properties of Ferroelectric Thin Films Having a Superlattice Structure of 2 Bi_3TiNbO_9 Units-1 $Bi_4Ti_3O_{12}$ Unit. *Appl. Phys. Lett.* **2003**, *83*, 1411–1413.
32. Gruverman, A.; Kalinin, S. V. Piezoresponse Force Microscopy and Recent Advances in Nanoscale Studies of Ferroelectrics. *J. Mater. Sci.* **2006**, *41*, 107–116.
33. Bousquet, E.; Dawber, M.; Stucki, N.; Lichtensteiger, C.; Hermet, P.; Gariglio, S.; Triscone, J. M.; Ghosez, P. Improper Ferroelectricity in Perovskite Oxide Artificial Superlattices. *Nature* **2008**, *452*, 732–736.
34. Osada, M.; Ebina, Y.; Fukuda, K.; Ono, K.; Takada, K.; Yamaura, K.; Takayama-Muromachi, E.; Sasaki, T. Ferromagnetism in Two-Dimensional $Ti_{0.8}Co_{0.2}O_2$ Nanosheets. *Phys. Rev. B* **2006**, *73*, 153301.
35. Osada, M.; Ebina, Y.; Takada, K.; Sasaki, T. Gigantic Magneto-Optical Effects in Multilayer Assemblies of Two-Dimensional Titania Nanosheets. *Adv. Mater.* **2006**, *18*, 295–299.